



Universiteit  
Leiden

The Netherlands

## **Anomalous diffusion of Dirac fermions**

Groth, C.W.

### **Citation**

Groth, C. W. (2010, December 8). *Anomalous diffusion of Dirac fermions*. *Casimir PhD Series*. Retrieved from <https://hdl.handle.net/1887/16222>

Version: Not Applicable (or Unknown)

License: [Leiden University Non-exclusive license](#)

Downloaded from: <https://hdl.handle.net/1887/16222>

**Note:** To cite this publication please use the final published version (if applicable).

# 1 Introduction

## 1.1 Normal and anomalous diffusion

Diffusion is the spreading of randomly moving particles from regions with higher concentration to regions with lower concentration. The first class of diffusive processes to have been recognized historically is now known under the name *normal diffusion*. Its signature is the linear growth with time of the mean squared displacement of a particle from its starting point,

$$\langle x^2 \rangle = Dt. \quad (1.1)$$

On long time scales all normal diffusive processes show the same behavior and microscopic details of particle dynamics play no role other than determining the value of the *diffusion coefficient*  $D$ .

The importance and generality of the concept of normal diffusion was recognized in the nineteenth century. One of the first milestones was the discovery of Brownian motion, the diffusion of particles suspended in a fluid, by Scottish botanist Robert Brown in 1827 [27]. It was subsequently realized that phenomena seemingly as different as the spreading of infected mosquitos [107] and the conduction of heat in solids can be described in terms of normal diffusion.

The driving force for diffusion need not be differences in concentration, but can also be a difference in potential energy. Electrical conduction in metals is usually also a normal diffusive process, driven by differences in electrical potential (since differences in electron concentration would violate charge neutrality) [39].

Though it is a remarkably general concept, normal diffusion fails to describe all diffusive phenomena. Since the 1970s, increasingly

processes were found in nature [125] where the mean squared displacement of a particle scales as a power of time different from unity,

$$\langle x^2 \rangle = Dt^\gamma, \quad \gamma \neq 1. \quad (1.2)$$

Examples include the foraging patterns of some animals [16], human travel behavior [26], and the spreading of light in a cloudy atmosphere [40]. This kind of diffusion has been termed *anomalous*, and can occur in two varieties: *subdiffusion*, where the particles spread with time arbitrarily slower than normal diffusion ( $\gamma < 1$ ), and *superdiffusion*, where they spread arbitrarily faster ( $\gamma > 1$ , with an upper limit  $\gamma = 2$  for ballistic motion without any scattering).

*Random walks* are stochastic processes in which particles move in a sequence of randomly directed steps. The lengths  $s$  of the steps and the duration  $\tau$  of a step are drawn from a probability distribution  $P(s, \tau)$ . (For simplicity, we assume an isotropic random walk, so  $P$  is independent of the direction of the step.) For a random walk to be normal, the variance  $\text{Var } s = \langle s^2 \rangle - \langle s \rangle^2$  of the step size has to be finite as well as the average duration  $\langle \tau \rangle$ . Then, according to the central limit theorem, the mean square displacement after time  $t$  will approach a normal distribution with variance  $(t/\langle \tau \rangle) \text{Var } s$ . This is the reason for the previously mentioned similarity of all diffusive processes.

If the requirements for a normal random walk are violated, the random walk will be anomalous and the scaling of the mean squared displacement will in general have a power law (1.2) with  $\gamma \neq 1$ . This can occur in several ways (See Ref. [145] for a detailed presentation).

Superdiffusion happens if the step size distribution  $P(s)$  has a heavy tail  $\propto 1/s^{1+\alpha}$  for large  $s$ , with  $0 < \alpha < 2$ . If the duration  $\tau = vs$  is simply proportional to the step size (with constant velocity  $v$ ) this leads to superdiffusive behavior with

$$\gamma = \max(3 - \alpha, 2). \quad (1.3)$$

Such an anomalous random walk is called a Lévy walk, after the French mathematician Paul Pierre Lévy. Alternatively, one



Figure 1.1: Two random walks of  $10^4$  steps each, characterized by a power-law-tailed step size distribution  $P(s) = \alpha/s^{\alpha+1}$  for  $s > 1$ ,  $P(s) = 0$  otherwise. The left walk is normal with  $\alpha = 3$  (Brownian walk), while the right one has  $\alpha = 3/2$  which makes it superdiffusive (Lévy walk). One clearly sees how individual steps play no dominant role in normal diffusion, while superdiffusion is dominated by individual long steps on all length scales.

might give each step the same duration  $\tau_0$ , independent of the step length. This so-called a Lévy flight has a divergent mean square displacement at any time  $t > \tau_0$ , and is therefore not physically realistic.

Fig. 1.1 shows two realizations of power-law-tailed random walks of which one is normal and one superdiffusive.

Another way to break normal diffusion is to have a step size distribution with a finite variance, but to associate with the steps durations drawn from a distribution with infinite mean. (See [11] for an introduction.) This leads to subdiffusive behavior characterized by  $\gamma < 1$ . Effectively, this happens if the random walk is performed on a fractal: a scale-invariant object of non-integer *fractal dimension*  $d_f$  embedded in Euclidean space of dimension  $d > d_f$ . The pieces of Euclidean space which are not part of the fractal present obstacles to the walker that are present at all length scales and slow down the diffusion. The value of  $\gamma < 1$  is specific

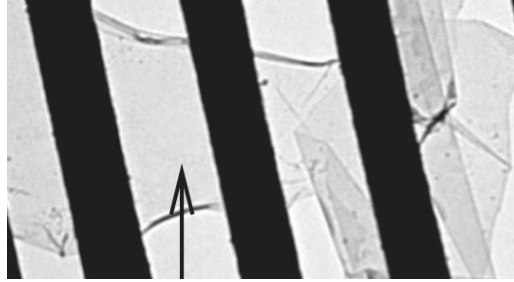


Figure 1.2: Bright-field transmission electron microscope image of a freely suspended graphene sheet. A homogeneous and featureless region of a monolayer graphene is indicated by the arrow; image from Ref. [93].

for each fractal and independent of the fractal dimension.

## 1.2 Dirac fermions and graphene

In 2004, Andre Geim and Konstantin Novoselov succeeded in isolating for the first time one atom thick flakes of graphite. Their achievement was awarded earlier this year with the Nobel prize in Physics.

This new material, named graphene, is made up of a single layer of carbon atoms arranged in a honeycomb lattice and was previously thought to be unstable and therefore only to exist as part of three-dimensional structures. With the wisdom of hindsight the existence of one atom thick crystals can be reconciled with theory [93]: slight corrugations of the monoatomic carbon film reinforce it against destructive thermal vibrations. Fig. 1.2 shows a photograph of a freely suspended piece of graphene.

The basic electronic properties of graphene which, mostly out of theoretical curiosity, had been studied since the 1940s [143, 91] could be verified by the experiments of Geim, Novoselov and others. The most striking feature is the double-cone shaped dispersion relation of electrons in graphene shown in the right panel of Fig.

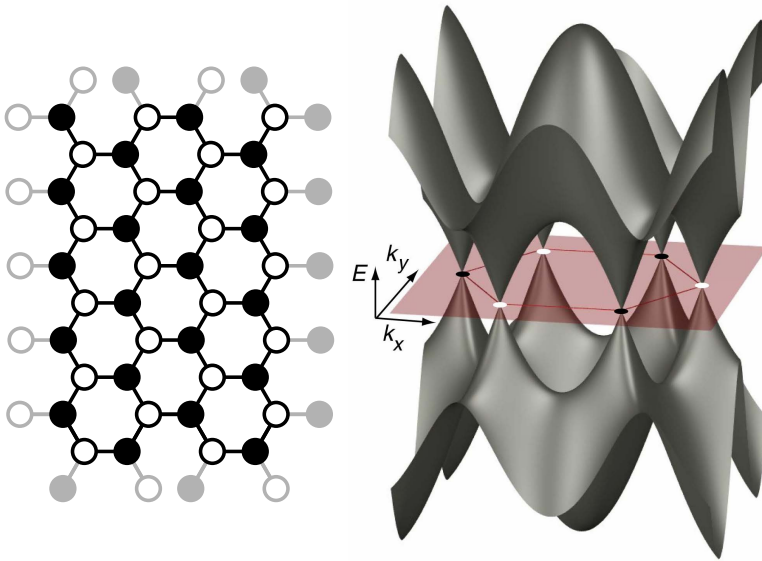


Figure 1.3: Left panel: Honeycomb lattice of carbon atoms in graphene. The unit cell contains two atoms, labeled A and B (open and closed circles). Right panel: Brillouin zone of graphene with a linear double cone spectrum at its corners; independent cones are indicated by open and closed circles. Illustration by C. Jozsa and B. J. van Wees.

1.3. As the velocity of the charge carriers is given by the derivative of the dispersion relation, we see that the speed of electrons in graphene is a constant independent of energy (for energies small enough such that the linear relation holds).

This is a most unusual property for particles in condensed matter physics. (Usually, the velocity increases with the square root of the energy.) It reminds of the energy-independent speed of photons, and indeed the low-energy long-wave length physics of electrons in graphene obeys the Dirac equation of relativistic quantum mechanics, or, more specifically, its two-dimensional massless version

$$-i\hbar v \begin{pmatrix} 0 & \partial_x - i\partial_y \\ \partial_x + i\partial_y & 0 \end{pmatrix} \begin{pmatrix} \Psi_A \\ \Psi_B \end{pmatrix} = E \begin{pmatrix} \Psi_A \\ \Psi_B \end{pmatrix}. \quad (1.4)$$

The  $A$  and  $B$  components of the wave function correspond to excitations on the two sublattices of the honeycomb lattice (see left panel of Fig. 1.3) and form a spin-like degree of freedom called pseudospin. The velocity  $v$  is the effective speed of light which in graphene is about  $10^6$  m/s or  $1/300$  of the true speed of light.

Definition of the vector of Pauli matrices  $\boldsymbol{\sigma} = (\sigma_x, \sigma_y, \sigma_z)$  allows to express Eq. (1.4) in the compact form

$$v\mathbf{p} \cdot \boldsymbol{\sigma} \psi = E\psi, \quad (1.5)$$

with the momentum operator  $\mathbf{p} = -i\hbar(\partial_x, \partial_y)$  and the spinor  $\psi = (\Psi_A, \Psi_B)$ . Electrons governed by Dirac equation are called Dirac fermions.

The Dirac equation has only a single *Dirac cone*, while the dispersion relation of graphene shown in the right panel of Fig. 1.3 has two independent cones called valleys. (Adjacent cones are independent, while next-nearest-neighbors are equivalent upon translation by a reciprocal lattice vector.) The existence of two independent cones is accounted for by the valley degree of freedom and the full<sup>1</sup> low energy physics has to be described by a four component spinor  $\mathbf{\Psi} = (\Psi_A, \Psi_B, -\Psi'_B, \Psi'_A)$  satisfying the four-dimensional Dirac equation

$$\begin{pmatrix} v\mathbf{p} \cdot \boldsymbol{\sigma} & 0 \\ 0 & v\mathbf{p} \cdot \boldsymbol{\sigma} \end{pmatrix} \mathbf{\Psi} = E\mathbf{\Psi}. \quad (1.6)$$

In the low-energy limit described by the Dirac equation the two valleys are decoupled, but in real graphene inter-valley scattering can occur by potential features which are sharp on the atomic scale.

The Dirac equation gives rise to unusual transport properties. Because the speed of Dirac particles is independent of their energy,

---

<sup>1</sup>The true spin degree of freedom of electrons is still missing, but it only weakly coupled to the dynamics and can be ignored.

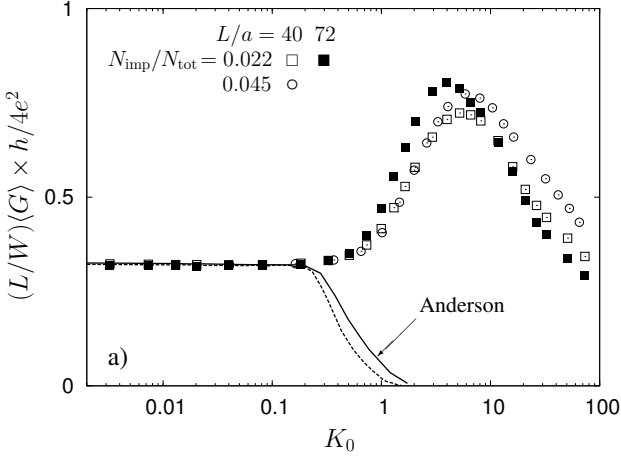


Figure 1.4: Computer simulation showing the dependence of the average conductance  $\langle G \rangle$  of a graphene sheet (length  $L$ , width  $W$ ) on the dimensionless disorder strength  $K_0$ . The data points are for different sample sizes and number of impurities  $N_{\text{imp}}$  per total number of lattice points  $N_{\text{tot}}$ . The conductance increases initially with increasing disorder strength, while in a conventional metal Anderson localization would suppress the conductance (solid and dashed curves). For strong disorder strengths intervalley scattering sets in, resulting in a suppression of the conductance. Figure from Ref. [116].

they cannot be stopped by a potential barrier [34, 64]. This has surprising consequences: adding disorder which is smooth on the scale of atoms to a graphene sample can enhance the conductivity [116] (Fig. 1.4). This behavior is in contrast to that of conventional metals, where disorder reduces the conductivity.

The deviations from normal diffusion in these systems have a quantum mechanical origin in the interference of electron waves. In conventional metals the interference is destructive on average, leading to a complete suppression of diffusion on long length

scales. This is the celebrated localization effect discovered by Philip Anderson in 1957 [9]. For Dirac fermions the interference is constructive on average, which is at the origin of the enhanced conductivity seen in Fig. 1.4.

### 1.3 Shot noise of subdiffusion

Conductance, the ratio between applied voltage and the resulting time-averaged current, is the basic quantity measured in electronic transport experiments. How does the conductance of a diffusive  $d$ -dimensional system scale with its linear size  $L$ ? For normal diffusion, the answer is given by Ohm's law,

$$G = \sigma L^{d-2}. \quad (1.7)$$

The proportionality constant  $\sigma$  is the conductivity.

Transport by anomalous diffusion is fundamentally different: the conductance depends on  $L$  with a different power than in Eq. 1.7. As a consequence, the conductivity becomes scale dependent.

In the case of subdiffusion on fractals the conductance scales as (reviewed in Refs. [135, 111])

$$G \propto L^{d_f-2/\gamma}, \quad (1.8)$$

with  $\gamma$  the exponent that governs the mean-square displacement in Eq. (1.2). Note that diffusion on a fractal is not just *normal* diffusion in a medium with non-integer dimension  $d_f$ . In that case, one would expect  $G$  to scale as  $L^{d_f-2}$ . Because  $\gamma$  is smaller than 1 for subdiffusion, conduction is suppressed stronger than would be expected solely on the basis of the fractal dimension.

Given the special scaling of conductance with length for subdiffusion, one might ask how other transport properties scale. While the time-averaged current determines the conductance, the time-dependent fluctuations determine the shot noise power  $S$ . In terms of the charge  $Q$  transmitted in a time  $\tau$ , one has

$$S = \lim_{\tau \rightarrow \infty} 2 \langle \delta Q^2 \rangle / \tau. \quad (1.9)$$

The shot noise power is proportional to the applied voltage and hence to the mean current

$$I = \lim_{\tau \rightarrow \infty} \langle Q \rangle / \tau. \quad (1.10)$$

The ratio  $F = S/2eI$  is called the Fano factor. The Fano factor is unity in the case where completely uncorrelated particles are transmitted. Then,  $Q$  is Poisson-distributed which leads to  $F = 1$ . A value  $F > 1$  indicates bunching of charge carriers (particles tend to arrive in groups more often than in the uncorrelated case), whereas  $F < 1$  is a signature of anti-bunching (particles arrive less often in groups). Anti-bunching of electrons is a consequence of the Pauli exclusion principle, which prevents two electrons to occupy the same quantum mechanical state. For normal diffusion the Pauli principle produces a Fano factor  $F = 1/3$  [18, 96].

What is the Fano factor for subdiffusion on fractals? Shot noise on fractals has been studied previously under circumstances that the Pauli principle is not operative, because the average occupation of a quantum state is much smaller than unity. (This is called a nondegenerate electron gas.) One example is the regime of high-voltage transport modeled by hopping conduction. Then  $I$  and  $S$  scale differently with  $L$ , so that the Fano factor is scale dependent. (See Fig. 1.5.) The Pauli principle is expected to govern the shot noise for diffusive conduction in the regime of low voltages and low temperatures, when the average occupation of a quantum state is of order unity (a degenerate electron gas).

This regime has become experimentally relevant in view of the discovery of electron and hole puddles in undoped graphene [89]. The puddles, shown in Fig. 1.6, form intertwined maze-shaped clusters doped positively (p) or negatively (n). The n-type region contains a degenerate electron gas and the p-type region contains a degenerate hole gas. The current flows with less resistance within an n-type or p-type region than across a p-n interface. Cheianov et al. modeled [89] this system by a random resistor network as illustrated in Fig. 1.7. The interconnected resistors in this model form *percolation clusters* which are fractals with  $d_f = 91/48$ .

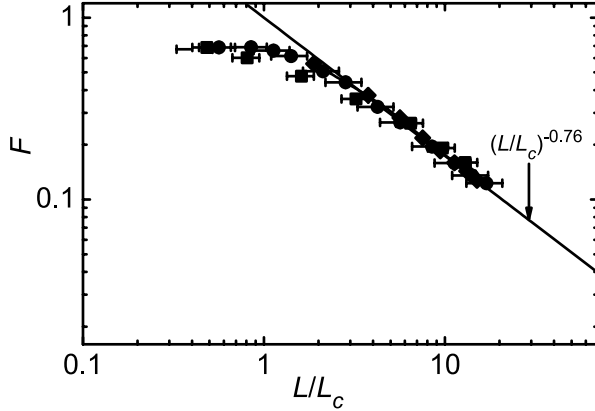


Figure 1.5: Fano factor as function of sample size from a Monte Carlo simulation of two-dimensional hopping through a disordered conductor. The Fano factor is scale dependent because the average current and the noise power scale with a different power of the sample size. Figure from Ref. [68].

Several experiments have studied the Fano factor of graphene recently. Measurements from two of these experiments, performed by Danneau et al. in Helsinki [37] and by DiCarlo et al. in Harvard [41] are shown in Figs. 1.8 and 1.9, respectively. In the Helsinki experiment the Fano factor depends strongly on doping, with a peak value of  $1/3$ , while the Harvard measurements show a doping-independent Fano factor of  $1/3$ . The theory for shot noise on a fractal developed in this thesis offers a way to reconcile these two conflicting experiments.

## 1.4 Discretization of the Dirac equation

The standard model for graphene is the tight-binding approximation, in which the hopping of electrons between overlapping orbitals of the atoms constituting the carbon sheet is directly con-

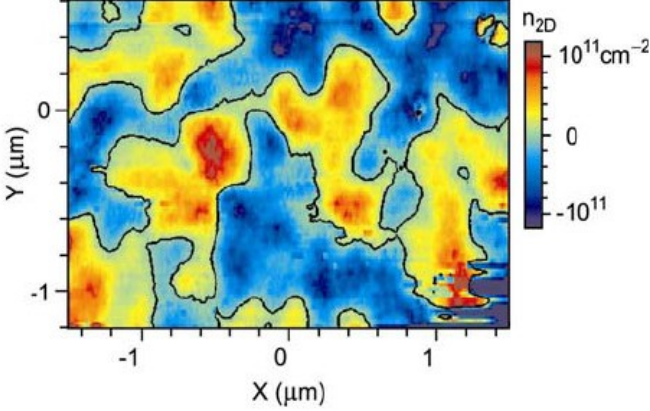


Figure 1.6: Experimentally determined color map of the spatial carrier density variations in a graphene flake. Blue regions correspond to hole doping (p-type) and red regions to electron doping (n-type). The black contour marks the p-n interface. Figure from Ref. [89].

sidered. This model is widely used to study the properties of graphene numerically. It can recover all electronic properties of the material, but is viable for small flakes only, as the computation times grow quickly with the number of atoms. To allow computer modeling of larger flakes of graphene and to probe the physics of a single Dirac cone, it would be useful to simulate the Dirac equation (1.4) directly, and not only as the low-energy limit of the tight-binding model. For this, the Dirac equation needs to be discretized, i.e. put on a lattice. This can be done in real space or in momentum space. The momentum space approach was developed in Refs. [13] and [99], while the real-space approach is developed in this thesis.

The discretization of the Dirac equation is notoriously difficult, because of the so-called *fermion doubling problem* [98]. The most straightforward way to discretize the Dirac equation in real space is to define the wave function  $\psi(x, y)$  on a rectangular grid with lattice

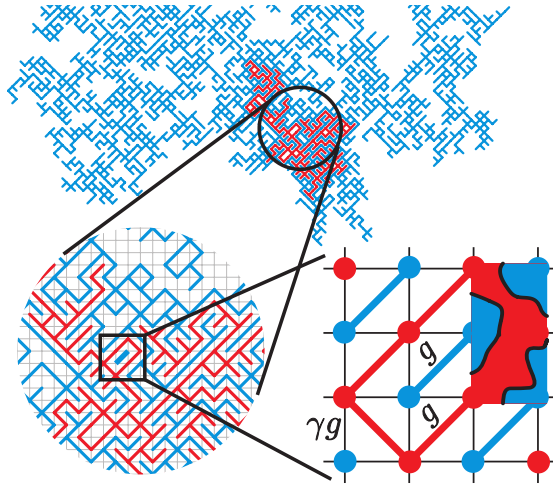


Figure 1.7: Random resistor network representation of a graphene sheet with average zero doping. The conductance is  $g$  within an n-type or p-type region (red or blue lines), and has a smaller value across a p-n interface. (The symbol  $\gamma$  used in this figure is unrelated to the random-walk exponent.) Figure from Ref. [35].

constant  $a$  and to replace the derivatives with finite differences,

$$\partial_x \psi \rightarrow \frac{\psi(x+a, y) - \psi(x-a, y)}{2a}, \quad (1.11)$$

$$\partial_y \psi \rightarrow \frac{\psi(x, y+a) - \psi(x, y-a)}{2a}. \quad (1.12)$$

This discretization fails to describe the physics of a single Dirac cone.

To see this, let us look at the dispersion relation of the discretized equation. For simplicity, we consider only plane waves moving in the  $x$  direction, so that  $k_y = 0$ . Such plane waves have the general form

$$\psi = \psi_0 e^{\pm i k_x x}. \quad (1.13)$$

Inserting this into the Dirac equation (1.4) with the substitutions

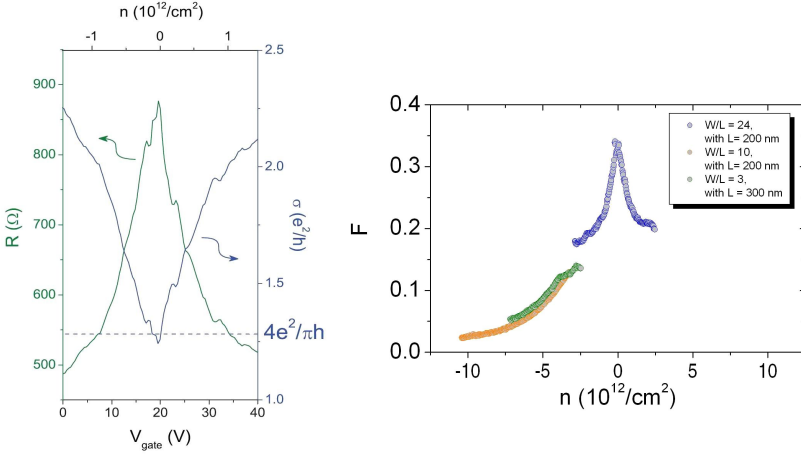


Figure 1.8: Results from a transport experiment performed by R. Danneau et al. on a graphene sheet. The measurements are consistent with theoretical predictions for ballistic transport at the Dirac point [141]. Left panel: Resistance and conductivity as a function of gate voltage and charge carrier density. The conductivity at the Dirac point reaches the expected value  $4e^2/\pi h$ . Right panel: Fano factor as function of charge carrier density. At the Dirac point, the value  $1/3$  is reached with  $F$  falling off for both positive and negative doping. Figures from Ref. [37].

(1.11) and (1.12) gives the dispersion relation

$$E = \pm \frac{\hbar v}{a} \sin ka, \quad (1.14)$$

plotted as the solid curve of Fig. 1.10.

We see that unphysical low-energy states, forming a second Dirac cone, have appeared around  $k_x a = \pm\pi, k_y = 0$ . There are two additional cones, one around  $k_x a = 0, k_y a = \pm\pi$ , and one around  $k_x a = \pm\pi, k_y a = \pm\pi$ , giving four in total in the first Brillouin zone. These additional states are due to the fact that the

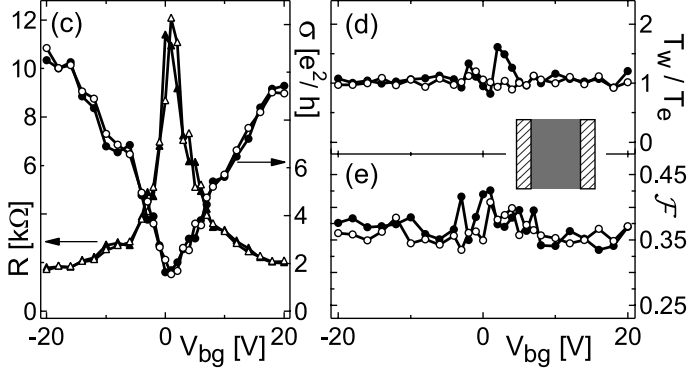


Figure 1.9: Results from a transport experiment performed by Di-Carlo et al. on a graphene sheet. Left panel: Resistance and conductivity as function of gate voltage. Right panel, lower part: Fano factor as function of gate voltage. The Fano factor has the value  $1/3$  independent of doping. Figure from Ref. [41].

Dirac equation (1.4) is a first order differential equation. To be able to evaluate the first derivatives at the same discretization points as the wave function, we had to take differences over two lattice sites in the difference operators (1.11) and (1.12). As a consequence, waves with a spatial period  $2\pi/|k_x|$  below  $4a$  are undersampled. This problem is specific for massless Dirac fermions. It does not arise for the Schrödinger equation, which massive fermions obey, as it is second order in space.

The fermion doubling problem also plagues the discretization of the Dirac equation in relativistic quantum mechanics. There exist ways to circumvent it by shifting the energy of the doubled states away from 0. One such method, the method of Wilson fermions [147], gives a mass to the Dirac fermions and thereby breaks a fundamental symmetry (so-called symplectic symmetry) needed to explain transport properties in graphene. An alternative method, known as the method of Kogut-Susskind fermions or as the staggered fermion method [71, 134, 22], preserves the symplec-

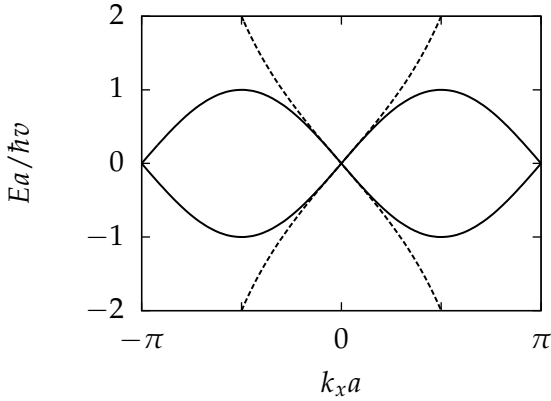


Figure 1.10: Solid curve: dispersion relation of the naively discretized Dirac equation showing *fermion doubling*: a second Dirac cone appears at  $k_x = \pm\pi$ . Dashed curve: dispersion relation of the Dirac equation discretized according to the method of staggered fermions. The energy of the unphysical states at  $k_x = \pm\pi$  has been shifted away to  $\pm\infty$ .

tic symmetry and is therefore the method which we will apply to graphene.

The dashed curve of Fig. 1.10 shows the dispersion relation of the Dirac equation discretized according to the staggered fermion method. The spurious Dirac cone has disappeared.

## 1.5 Topological insulators

In 1980 Klaus von Klitzing discovered that the conductance of thin semiconductor layers at low temperatures and large perpendicular magnetic fields is quantized in integer multiples of the conductance quantum  $e^2/h$  [69]. The mechanism for this *quantum Hall effect* is illustrated in the left panel of Fig. 1.11 and can be described as follows: Under the influence of the magnetic field the

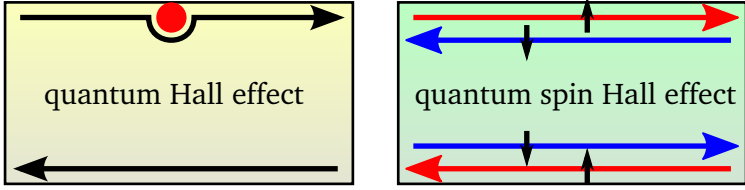


Figure 1.11: Left panel: the quantum Hall effect has a single conducting channel along the edge. Because movement in the channel is only possible in a single direction, electrons cannot be scattered back by impurities (an impurity is symbolized by the red dot). Right panel: the quantum spin Hall effect has two spin-polarized channels per edge of opposite spin (the spin orientation is indicated by the short black arrows), propagating in opposite directions. Backscattering is now forbidden by Kramers theorem.

electrons move in quantized circular orbits (Landau levels), making the bulk of the sample insulating. Electrons at the edges of the samples cannot perform full circles and are forced to “skip along the edge”. This leads to the appearance of conducting edge states which propagate in a single direction only. Backscattering requires scattering to the opposite edge, which is strongly suppressed if the sample is sufficiently wide. Due to the absence of backscattering, the transmission probability is unity for each edge channel at the Fermi level. Each fully transmitted edge channel contributes  $e^2/h$  to the conductance, leading to the observed quantization.

An analogous quantization of the conductance in zero magnetic field occurs in a new class of materials known as topological insulators [50, 108]. This so-called *quantum spin Hall effect* requires spin-orbit coupling to produce an unusual band structure (shown schematically in Fig. 1.12) that leads to the appearance of an insulating bulk and conducting edge channels. There are now two counterpropagating edge channels at each edge, so backscattering

would not require scattering to the opposite edge. The reason that backscattering is still forbidden is a rather subtle consequence of time reversal symmetry.

Since a magnetic field is absent, the system is time reversal invariant – its Hamiltonian  $H$  is unchanged by the anti-unitary time-reversal operator  $\Theta$ :

$$\Theta H \Theta^{-1} = H. \quad (1.15)$$

Because the electrons have spin  $1/2$ , the operator  $\Theta^2$  is equal to  $-1$ . In this case, Kramers theorem states that all electron states are at least twofold degenerate: Let us consider a state  $\psi$  at energy  $E$ ,

$$H\psi = E\psi. \quad (1.16)$$

Because of Eq. (1.15), the state  $\Theta\psi$  has the same energy  $E$  as  $\psi$ . The state  $\Theta\psi$  cannot be equivalent to  $\psi$ , as assuming that  $\Theta\psi$  differs from  $\psi$  just by a phase factor  $e^{i\delta}$  leads to

$$\Theta^2\psi = \Theta e^{i\delta}\psi = e^{-i\delta}\Theta\psi = e^{-i\delta}e^{i\delta}\psi = \psi, \quad (1.17)$$

which contradicts the previously stated  $\Theta^2 = -1$ . (The second equality in Eq. (1.17) is due to  $\Theta$  being antiunitary.)

Kramers theorem tells us that there should be at least two states at each energy. This forbids scattering between the counterpropagating edge channels, because that would remove the crossing at zero momentum in Fig. 1.12 and thus remove the degeneracy.

The spectrum near the crossing looks similar to that near the Dirac point in graphene (cf. Fig. 1.10), and indeed, the electrons moving in the edge channels are governed by a one-dimensional version of the Dirac equation (1.4). Topological insulators are therefore an alternative source of Dirac fermions and many of the techniques developed in the study of graphene can be applied to this new class of materials.

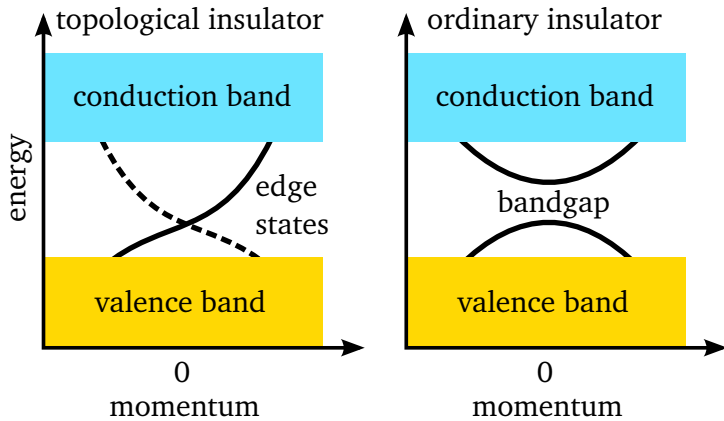


Figure 1.12: Schematic comparison of the band structure of a topological insulator (left panel) and an ordinary insulator (right panel). Both have an insulating bulk, but the topological insulator has conducting edge states inside the band gap. The crossing of the edge states cannot be avoided because that would violate Kramers theorem (requiring twofold degenerate energy levels).

## 1.6 Outline of this thesis

The research presented in the following chapters concerns the anomalous diffusion of particles in general and Dirac fermions in particular. One area of focus are the implications of anomalous diffusion for electronic shot noise. Novel methods for simulation of Dirac fermions (which might exhibit anomalous diffusion) were developed. Finally, some aspects of transport of Dirac fermions in topological insulators were studied numerically and analytically.

### Chapter 2: Electronic shot noise in fractal conductors

Motivated by the experiments mentioned in Sec. 1.3, in Chapter 2 we study the shot noise of subdiffusion on fractals. The two kinds of fractals we consider are the Sierpiński gasket (a regular fractal)

and random planar resistor networks which arise from a model of graphene. We determine the scaling with size  $L$  of the shot noise power  $S$  due to elastic scattering in a fractal conductor. We find a power-law scaling  $S \propto L^{d_f - 2/\gamma}$ , with an exponent depending on the fractal dimension  $d_f$  and the anomalous diffusion exponent<sup>2</sup>  $\gamma$ . This is the same scaling as the time-averaged current  $I$ , which implies that the Fano factor  $F = S/2eI$  is scale independent. We obtain a value  $F = 1/3$  for anomalous diffusion that is the same as for normal diffusion, even if there is no smallest length scale below which the normal diffusion equation holds. The fact that  $F$  remains fixed at  $1/3$  as one crosses the percolation threshold in a random-resistor network may explain measurements of a doping-independent Fano factor in a graphene flake [41].

### Chapter 3: Nonalgebraic length dependence of transmission through a chain of barriers with a Lévy spacing distribution

In Chapter 3 we analyze transport through a linear chain of barriers with independent spacings  $s$  drawn from a heavy-tailed Lévy distribution. We are motivated by the recent realization of a “Lévy glass” [15] (a three-dimensional optical material with a Lévy distribution of scattering lengths) of which our system is a one-dimensional analogue. The step length distribution of particles in our system also has a heavy tail,  $P(s) \propto s^{-1-\alpha}$  for  $s \rightarrow \infty$ , but strong correlations exist between subsequent steps because the same space between two barriers will often be traversed back after a particle gets scattered by a barrier. We show that a random walk along such a sparse chain is not a Lévy walk because of these correlations. Thus, by working in the lowest possible dimension, we can provide a worst-case estimate for the effect of the correlations in higher dimensions.

We calculate all moments of conductance (or transmission), in the regime of incoherent sequential tunneling through the barriers.

---

<sup>2</sup>In Chapter 2 the symbol  $\alpha$  is used for a differently defined anomalous diffusion exponent:  $\alpha = 1/\gamma - 2$ .

The average transmission from one barrier to a point at a distance  $L$  scales as  $L^{-\alpha} \ln L$  for  $0 < \alpha < 1$ . The corresponding electronic shot noise has a Fano factor that approaches  $1/3$  very slowly, with  $1/\ln L$  corrections.

## **Chapter 4: Finite difference method for transport properties of massless Dirac fermions**

As shown in Sec. 1.4, a straightforward discretization of the massless Dirac equation fails because of the fermion doubling problem. In Chapter 4 we adapt a finite difference method of solution, developed in the context of lattice gauge theory, to the calculation of electrical conduction in a graphene sheet or on the surface of a topological insulator. The discretized Dirac equation retains a single Dirac point (no fermion doubling), avoids intervalley scattering as well as trigonal warping (a triangular distortion of the conical band structure that breaks the momentum inversion symmetry), and thus preserves the single-valley time reversal symmetry (= symplectic symmetry) at all length scales and energies. This comes at the expense of a nonlocal finite difference approximation of the differential operator. We demonstrate the symplectic symmetry by calculating the scaling of the conductivity with sample size, obtaining the logarithmic increase due to antilocalization. We also calculate the sample-to-sample conductance fluctuations as well as the shot noise power, and compare with analytical predictions.

Our numerical results are in good agreement with a recent theory of transport in smoothly disordered graphene by Schuessler et al. [122]. Fig. 1.13 compares their analytical results (solid curve) with our numerical data (rectangles). The same numerical results were used to prepare Fig. 4.12.

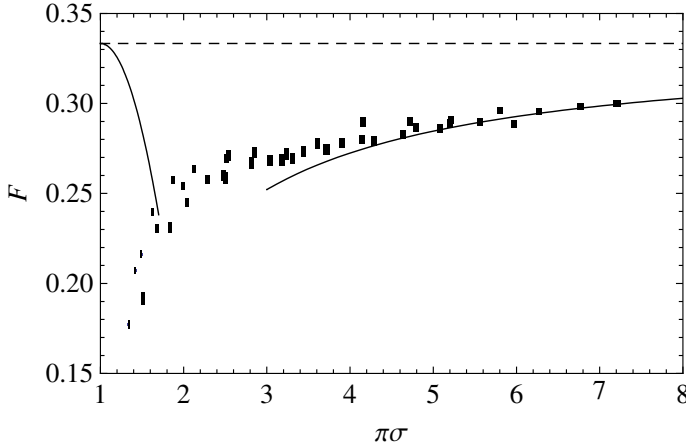


Figure 1.13: Fano factor as a function of conductivity for smoothly disordered graphene. The solid curves show ballistic and diffusive results of Ref. [122]. The dashed line corresponds to the asymptotic value  $F = 1/3$ . The solid rectangles are our numerical results, obtained with the method of Chapter 4. The size of rectangles corresponds to the statistical error estimate. Figure from Ref. [122].

## Chapter 5: Switching of electrical current by spin precession in the first Landau level of an inverted-gap semiconductor

In Chapter 5 we show how the quantum Hall effect in a two-dimensional topological insulator can be used to inject, precess, and detect the electron spin along a one-dimensional pathway. The restriction of the electron motion to a single spatial dimension ensures that all electrons experience the same amount of precession in a parallel magnetic field, so that the full electrical current can be switched on and off. As an example, we calculate the magnetoconductance of a  $p$ - $n$  interface in a HgTe quantum well and show how it can be used to measure the spin precession due to bulk inversion asymmetry. A realization of this experiment would

provide a unique demonstration of full-current switching by spin precession.

## **Chapter 6: Theory of the topological Anderson insulator**

In Chapter 6 we present an effective medium theory that explains the disorder-induced transition into a phase of quantized conductance, discovered in computer simulations of HgTe quantum wells [81]. Depending on the width of their innermost layer, such quantum wells are two-dimensional topological insulators or ordinary insulators. Our theory explains how the combination of a random potential and quadratic corrections  $\propto p^2\sigma_z$  to the Dirac Hamiltonian can drive an ordinary band insulator into a topological insulator (having conducting edge states). We calculate the location of the phase boundary at weak disorder and show that it corresponds to the crossing of a band edge rather than a mobility edge. Our mechanism for the formation of a topological Anderson insulator is generic, and would apply as well to three-dimensional semiconductors with strong spin-orbit coupling. It has indeed been adapted to that case recently [49].